AIMS Mathematics, 11(5): 12977–13007.
DOI: 10.3934/math.2026534
Received: 19 January 2026
Revised: 07 April 2026
Accepted: 20 April 2026
Published: 11 May 2026

https://www.aimspress.com/journal/Math

Research article

Nonlinear dynamics and bifurcation analysis of a PPF-controlled broadband Piezoelectric energy harvester

Moamen Wafaie[1], Rageh K. Hussein[2], Ashraf Taha EL-Sayed[1,*] and Fatma Taha El-Bahrawy[1]

[1] Department of Basic Science, Modern Academy for Engineering and Technology, Elmokattam, Cairo 11439, Egypt
[2] Physics Department, College of Science, Imam Mohammad Ibn Saud Islamic University (IMSIU), Riyadh 11623, Saudi Arabia

* **Correspondence:** Email: atelsayed@eng.modern-academy.edu.eg; ashraftaha211@yahoo.com.

Abstract: In this paper, we present a comprehensive analytical–numerical investigation of the nonlinear dynamics and bifurcation behavior of a broadband piezoelectric energy harvester (PEH) integrated with a Positive Position Feedback (PPF) control strategy. The novelty of this work lies in the development of a unified framework that captures the coupled effects of primary and internal resonances in the presence of active control. The governing nonlinear equations of motion were solved analytically using the second-order Multiple Scales Perturbation Technique (MSPT), yielding accurate approximate solutions and frequency–response relationships. The proposed approach provided a rigorous analytical treatment of the controlled nonlinear system. It revealed the underlying mechanisms governing vibration suppression and stability enhancement. Furthermore, bifurcation analysis was conducted to identify multistability, jump phenomena, and transitions between stable and unstable solutions as system and control parameters vary. The analytical predictions were validated through numerical simulations using MATLAB and MAPLE, showing excellent agreement in frequency–response curves, time histories, and phase portraits. The results demonstrated that the PPF controller significantly improves the system's dynamic performance by suppressing nonlinear oscillations, mitigating jump phenomena, reducing settling time, and stabilizing the response, leading to more stable and favorable operating regimes for effective energy harvesting. Overall, this study provides new insights into the design and control of nonlinear piezoelectric energy harvesting systems with potential applications in self-powered sensing and smart vibration control systems.

Keywords: nonlinear dynamics; bifurcation analysis; multiple scales method; stability analysis; positive position feedback control; Piezoelectric energy harvesting
Mathematics Subject Classification: 34A34, 37N35, 70J99, 70K20, 74H10

1. Introduction

Broadband piezoelectric energy harvesters (PEHs) have attracted significant attention due to their ability to convert ambient mechanical vibrations into electrical energy over a wide frequency range. These systems play a crucial role in powering low-energy electronic devices, particularly in environments with variable and unpredictable vibration sources. Their advantages include reduced reliance on batteries, compact size, and ease of integration into smart and self-powered systems.

Researchers have focused on improving the performance of broadband PEHs through structural design, nonlinear dynamics, and control strategies. For instance, Hao et al. [1] investigated rainfall-driven piezoelectric harvesters and demonstrated the influence of droplet impact parameters on energy output. Zhao et al. [2] proposed a multimodal circular-array structure and analyzed the effects of geometric configurations on harvesting efficiency. Wu et al. [3] introduced an elastic amplification mechanism for multidirectional vibration harvesting. [4] presents an innovative piezoelectric energy harvester with variable geometry and rotating MFC fiber orientation to improve energy conversion under wideband excitations. The FE results are validated using COMSOL® simulations and experimental data. In [5], internal resonance is introduced as an effective technique for enhancing vibration-based energy harvesting in nonlinear electromagnetic systems with snap-through nonlinearity. The multiple scales method reveals two nonlinear amplitude-frequency response peaks bending in opposite directions under primary and 2:1 internal resonance conditions. The analytical results are verified numerically, confirming the effectiveness of nonlinear piezoelectric energy harvesters with mono-stable and multi-stable configurations. The study compares cantilever-based harvesters with magnetic interactions, showing that system stability depends on the balance between vertical magnetic force and equivalent linear elastic force [6]. A nonlinear auto-parametric piezoelectric energy harvester with a nonlinear energy sink is proposed to achieve stable broadband energy harvesting and suppress chaotic vibrations. The results show improved stability and energy conversion efficiency through effective chaos control [7]. In [8], a Galfenol-based magnetostrictive energy harvester is modeled to investigate nonlinear magnetic and electromechanical behaviors under different excitation conditions. In [9], a nonlinear hybrid system combining a piezoelectric energy harvester, pendulum, and Duffing oscillator is controlled using a novel PHPD technique for simultaneous vibration suppression and energy harvesting. The results demonstrate significant vibration reduction and improved system stability.

To reduce vibrations at multiple resonance frequencies in buildings, Multimode Modified Positive Position Feedback (MMPPF) is suggested [10]. In [11], a multimode positive position feedback (MMPPF) control technique is proposed to suppress high-amplitude vibrations of a flexible beam under external excitation. The results confirm effective vibration reduction and wide suppression bandwidth, validated numerically. [12] proposes an active modal TMD control strategy for vibration suppression using a closed-loop approach based on conventional TMD theory. The method acts independently on each modal coordinate and is compared with existing techniques such as PPF and IMSC. [13] experimentally investigates PPF and NDF controllers for vibration suppression of a flexible

manipulator with a piezoelectric actuator. The results show that the NDF controller provides better vibration attenuation, shorter settling time, and greater robustness to natural frequency variations than the PPF controller. [14–18] focus on active vibration control of smart structures using piezoelectric actuators and materials. Various control strategies, including feedback, adaptive, and modified acceleration feedback controls, are proposed to enhance vibration attenuation, stability, and structural performance. [19] introduces a quantitative approach for detecting P-bifurcations in stochastic systems using Shannon entropy. The proposed method is applied to the noisy DVDP oscillator and compared with traditional D-bifurcation and qualitative P-bifurcation analyses.

[20] investigates the nonlinear dynamics of a forced and self-excited cantilever beam coupled with a PPF controller. The MSPT is used to derive the approximate solution and analyze stability, while the effects of controller parameters on vibration reduction are examined and validated numerically. [21] analyzes a PPF controller for suppressing vibrations of a nonlinear dynamic system under primary and 1:1 internal resonance conditions using the multiple-scale method and bifurcation analysis. [22] proposes two PPF controllers to reduce longitudinal and angular vibrations of a nonlinear spring pendulum system under simultaneous primary and internal resonance conditions, with the system behavior analyzed using MSPT. [23,24,26] apply perturbation techniques such as MTSP and MSPT to analyze and control nonlinear dynamical systems. The studies investigate the effects of parameter variations on vibration amplitudes and system behavior using frequency-response equations and numerical simulations through MATLAB and MAPLE programs. [25] investigates the dynamical behavior and stability of systems using phase portraits, bifurcation diagrams, Lyapunov spectra, and Poincaré maps, highlighting applications of piezoelectric transducers in engineering and medical devices. [27] studies system dynamics and stability through phase portraits, bifurcation diagrams, Lyapunov spectra, and Poincaré maps, highlighting applications of piezoelectric transducers. [28] investigates a Duffing oscillator with delayed velocity feedback and shows that delayed control improves stability and delays Hopf bifurcation. [29] analyzes a nonlinear broadband piezoelectric energy harvester with adjustable mono- and bistable configurations using the harmonic balance method.

Advancements in nonlinear vibration analysis have highlighted the significance of transverse nonlinear responses in complex engineering systems. The researchers in [33] demonstrated that fluid–structure interaction (FSI) can induce rich nonlinear dynamics and instability in fluid-conveying pipes, particularly under varying geometric and material conditions. The study also emphasized the effectiveness of advanced control strategies and hybrid energy harvesting techniques in suppressing vibrations and enhancing energy conversion efficiency. These developments further confirm the importance of incorporating nonlinear dynamics and control mechanisms in modern energy harvesting systems, which directly supports the motivation and framework of this study.

Developments in advanced control strategies have demonstrated the effectiveness of observer-based active disturbance rejection control (ADRC) in suppressing vibrations in complex nonlinear systems. By utilizing an intermediate observer, such methods can estimate system states and unknown disturbances, ensuring robust stabilization even in the presence of uncertainties, time delays, and external excitations. These features make ADRC-based approaches particularly suitable for nonlinear vibration control and energy harvesting systems, where uncertainties and strong nonlinearities play a significant role. This further motivates the use of efficient control strategies, such as the one proposed in this study, to enhance system stability and vibration attenuation [34]. Researchers have investigated the nonlinear vibration behavior of functionally graded piezoelectric structures, such as multi-layered nanoplates resting on elastic foundations. For instance, Fang et al. (2024) [35] analyzed the nonlinear

dynamics of a five-layered piezoelectric semiconductor nanoplate using Hamilton's principle and nonlocal elasticity theory, demonstrating that material gradation and foundation parameters significantly influence the vibration characteristics. However, these researchers mainly focus on structural and material design aspects, whereas we adopt a control-oriented approach to regulate nonlinear dynamics and improve system performance.

From an engineering perspective, broadband piezoelectric energy harvesters have significant potential applications in various fields, including aerospace structures, flexible spacecraft, micro-electromechanical systems (MEMS), and self-powered sensing devices. In such systems, vibration suppression and energy harvesting are often required simultaneously, particularly in environments where external power sources are limited.

Compared to conventional passive control techniques, such as tuned mass dampers, the proposed approach offers improved adaptability and effectiveness under varying excitation conditions. Moreover, unlike traditional active control systems that require continuous external power, the integration of piezoelectric energy harvesting introduces the possibility of utilizing ambient energy to support or complement the control process.

Therefore, the proposed PPF-based controlled PEH system provides a dual-function solution by combining vibration mitigation with energy harvesting capability, which represents a significant advantage over purely passive or purely active control strategies.

It should be noted that the comparison presented in this study is primarily conceptual, focusing on the dynamic performance of the system. Unlike passive control methods, which are typically limited to fixed operating conditions, the proposed PPF-based approach offers improved adaptability to varying excitation scenarios. Moreover, in contrast to conventional active control systems that rely entirely on external power sources, the integration of piezoelectric energy harvesting provides a potential pathway toward energy-assisted or self-powered control. To further clarify the advantages of the proposed approach, a conceptual comparison with conventional passive and active control strategies is summarized in Table 1.

The primary contribution of this work is the development of a nonlinear controlled structure for vibration mitigation in a two-degree-of-freedom (2DOF) physical oscillator integrated with a piezoelectric energy harvester. In this framework, a Positive Position Feedback (PPF) controller is incorporated to enhance system stability, reduce vibration amplitudes, and significantly shorten the settling time. The novelty of this study lies in combining nonlinear control design with advanced analytical techniques to investigate the system under simultaneous primary and internal resonance conditions. Specifically, the second-order Multiple Scales Perturbation Technique (MSPT) is employed to derive approximate analytical solutions, while bifurcation analysis is used to reveal complex dynamical behaviors, including multi-stability and jump phenomena. In addition, the proposed analytical results are validated through numerical simulations using the fourth-order Runge–Kutta method, demonstrating excellent agreement between theoretical and numerical findings.

Unlike many researchers who focus on enhancing energy-harvesting performance through structural nonlinearities, such as bistros or multi-stable mechanisms, we adopt a control-oriented perspective. The proposed approach does not modify the physical harvesting mechanism but regulates the system dynamics via a PPF controller. This strategy enables improved vibration suppression and response stabilization, which are essential factors influencing the effectiveness and robustness of energy harvesting systems under nonlinear resonant conditions.

System stability is rigorously examined using the Routh–Hurwitz criterion, and a detailed

parametric study is conducted to evaluate the influence of key system parameters. Overall, this work provides new insights into the integration of nonlinear control and analytical modeling for broadband piezoelectric energy harvesting systems.

Table 1. Conceptual comparison between vibration control strategies.

Feature	Passive Control (e.g., TMD)	Active Control (Traditional)	Proposed PPF-based PEH System
Adaptability to excitation	Limited	High	High
External power requirement	Not required	Required	Required
Implementation complexity	Low	High	High
Vibration suppression efficiency	Moderate	High	High
Energy harvesting capability	Not available	Not available	Not available
Suitability for broadband systems	Limited	Moderate	Moderate

It should be noted that this comparison is qualitative and aims to highlight the general characteristics of each approach.

2. Explanation of the structure

A thin piezoelectric beam equipped with electrodes and connected to an external resistive load is subjected to an initial axial compressive force applied through a spring mechanism, as illustrated in Figure 1. This configuration represents a bistable piezoelectric energy harvester. The applied compressive force drives the beam into a post-buckled configuration, resulting in mechanical bistability characterized by two stable equilibrium states separated by an unstable equilibrium path.

Under external periodic excitation at the support, the system may undergo snap-through transitions between these stable states, leading to large-amplitude nonlinear transverse oscillations. These snap-through events significantly increase the mechanical strain experienced by the piezoelectric layer, thereby enhancing the electromechanical coupling and increasing the amount of energy converted into electrical power across the load resistance.

In Figure 1, the blue curve represents the unstable equilibrium path corresponding to an equivalent monostable system, while the red curves denote the stable equilibrium branches associated with the bistable configuration. Overall, the combination of bistable structural behavior and piezoelectric transduction enables efficient energy harvesting by exploiting large-strain nonlinear oscillations, particularly under low-frequency or low-amplitude environmental excitations.

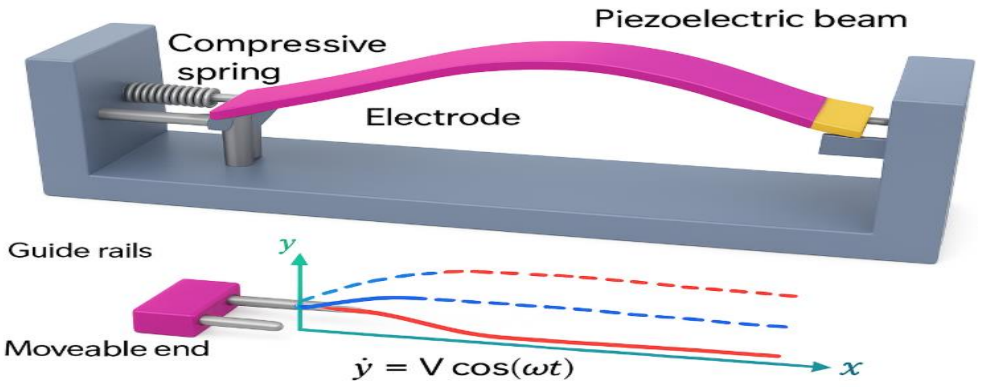

Figure 1. The suggested nonlinear PEH's schematic shows the stable and unstable locations with red and blue dashed lines.

3. The procedure used by a structure with PPF control

3.1. Electromechanical interpretation of the system

In piezoelectric energy harvesting systems, the electrical output is inherently coupled with the mechanical response of the structure. The generated voltage is directly proportional to the structural deformation, while the electrical current depends on the rate of change of this deformation.

Accordingly, the electromechanical coupling can be expressed in a simplified form as:

$$V(t) \propto \eta(t) \quad \text{and} \quad I(t) \propto \frac{d\eta(t)}{dt}.$$

This implies that any modification in the displacement η and its time derivative, such as those induced by the PPF control strategy, will directly influence the generated electrical response.

Therefore, improving the system's dynamic behavior, including vibration suppression, elimination of jump phenomena, and faster convergence to steady state, enhances the stability and effectiveness of the energy harvesting process, even when the electrical circuit is not explicitly modeled.

This simplified representation is widely adopted in theoretical studies to capture the essential coupling between mechanical and electrical domains.

The researchers in [34] deduce the nonlinear second-order ordinary differential equation that accounts for the PEH's equation of motion as follows:

$$\ddot{\eta} + 2\varepsilon\omega_1\xi_1\dot{\eta} + \omega_1^2\eta + \varepsilon\beta\left(\eta\dot{\eta}^2 + \eta^2\ddot{\eta}\right) + \varepsilon\alpha_1\eta^3 - \varepsilon\alpha_2 y = \varepsilon f\cos(\Omega t), \tag{1-a}$$

$$\dot{v} + \delta v + \alpha_3\dot{\eta} = 0. \tag{1-b}$$

The following is an approximate mathematical prescription for the PPF damper, which is made for tightening the control over the PEH:

$$\ddot{\eta} + 2\varepsilon\omega_1\xi_1\dot{\eta} + \omega_1^2\eta + \varepsilon\beta\left(\eta\dot{\eta}^2 + \eta^2\ddot{\eta}\right) + \varepsilon\alpha_1\eta^3 - \varepsilon\alpha_2 v = \varepsilon f\cos(\Omega t) + \varepsilon\gamma_1 z, \tag{2-a}$$

$$\dot{v} + \delta v + \alpha_3\dot{\eta} = 0, \tag{2-b}$$

$$\ddot{z} + 2\varepsilon\omega_2\xi_2\dot{z} + \omega_2^2 z = \varepsilon\gamma_2\eta, \tag{2-c}$$

where η is the primary mass displacement, v the secondary part of the system, z is the internal PPF/feedback state, α_1 is the linear stiffness of the primary system, α_2 is the linear stiffness of the secondary part of the system, ξ_1 is the damping ratio of the primary system, ξ_2 is the damping ratio of the absorber, β is the cubic stiffness coefficient, f is the forcing amplitude, Ω is the forcing frequency, ε is a small perturbation parameter, γ_1, γ_2 are the coupling coefficients, δ is internal damping of the secondary part of the system, and α_3 is the controller gain.

3.2. Electromechanical interpretation of the system

In PEH systems, the electrical output is inherently coupled to the mechanical response. The generated current is proportional to the rate of change of strain, while the voltage is directly related to the induced deformation. Therefore, improving the system's dynamic behavior, such as reducing undesirable oscillations and stabilizing the response, enhances the effectiveness and reliability of the energy harvesting process, even when the electrical circuit is not explicitly modeled.

3.3. Achievement in time history absent control

The structure's time history is effective at the principal resonance, in the absence of a controller, and with the controller studied at the primary resonance $\Omega \cong \omega_1$ and internal resonance $\omega_2 \cong \omega_1$ with the next parameter values.

The fourth-order Runge-Kutta procedure (ode45 in MATLAB) [32] is used to find the solution numerically of the provided uncontrolled system of Eqs (1-a) and (1-b) to examine the actions of the dynamic system.

Table 2. The specified parameter measurements.

Parameters symbol	Values	Parameters symbol	Values	Parameters symbol	Values
β	0.1	α_2	0.8	Ω	ω_1
ω_1	1	α_3	1	α_1	1
ω_2	ω_1	f	0.5	δ	0.4
γ_1	15	ξ_1	0.05		
γ_2	20	ξ_2	0.8		

We study one of the most important resonance cases, simultaneous primary and 1:1 internal resonance, to gain more knowledge of the system's dynamical history records (1) and (2), with and without the PPF controller. The earlier stated dynamical algorithm's repetition has been quantitatively calculated using RK-4, with the fundamental presumptions; $\eta(0) = 1.2; \dot{\eta}(0) = (0);\ \nu(0) = 0;\ \dot{\nu}(0) = 0$. In Figure 2, both oscillators have an initial transient phase in which the amplitude decays significantly due to the combined effects of linear and nonlinear damping, as investigations demonstrate. After the transient phase, the system settles into a steady periodic motion with a reduced amplitude. The spiraling trajectories in the phase plots (subplots b and d) that converge to a closed loop show the change from transient behavior to a stable limit cycle. Additionally, the absorber response (subplots c and d) reveals a unique energy-transfer process from the primary system to the auxiliary mass, illustrating the effectiveness of the nonlinear coupling in lowering vibrations. The results in Figure 3 indicate rapid attenuation of the transient motion followed by a stable periodic response for all three coordinates after adding PPF control. The phase portraits confirm this behavior through inward spiraling motions that settle into closed orbits, reflecting the combined influence of damping and nonlinear coupling within the system.

To further clarify the effect of the control strategy on the system dynamics, a comparison of the phase portraits before and after control is presented in Figure 4. In the uncontrolled case, the system exhibits large-amplitude oscillatory trajectories, indicating sustained nonlinear vibrations. In contrast, after applying the control mechanism, the phase trajectories rapidly converge toward a stable equilibrium point, reflecting strong damping and effective suppression of oscillations. This transition demonstrates the capability of the proposed control strategy to stabilize the system and significantly reduce vibration amplitudes, which is essential for achieving more stable and efficient energy harvesting performance. This comparison highlights the transition from oscillatory behavior to a stable fixed-point response, confirming the effectiveness of the control mechanism in eliminating nonlinear vibrations and enhancing system stability.

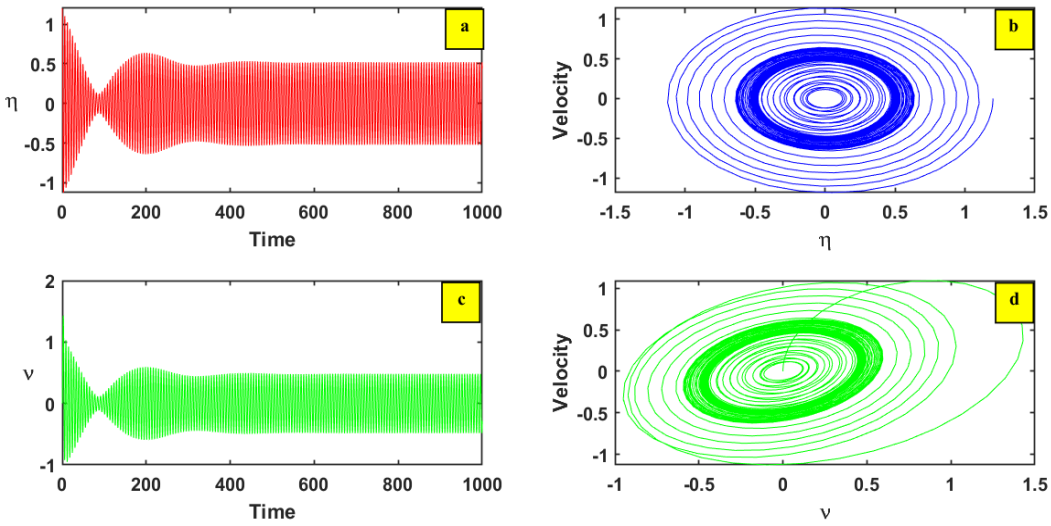

Figure 2. (a) Time responses and phase portraits of the primary system η. (c) The second part of the system ν. (b, d) The corresponding spiral trajectories converging to stable limit cycles.

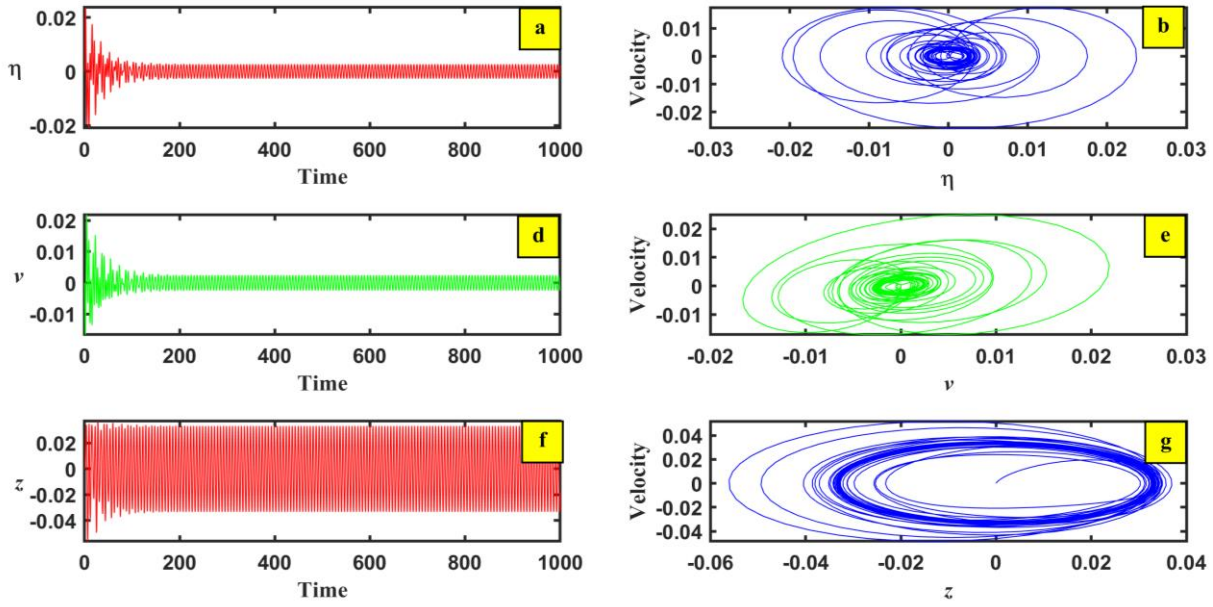

Figure 3. Time responses and phase portraits of the primary displacement η, the second part of the system ν, and the damper z. (a, c, e) The decay of transient oscillations. (b, d, f) The corresponding spiral trajectories converge toward stable limit cycles.

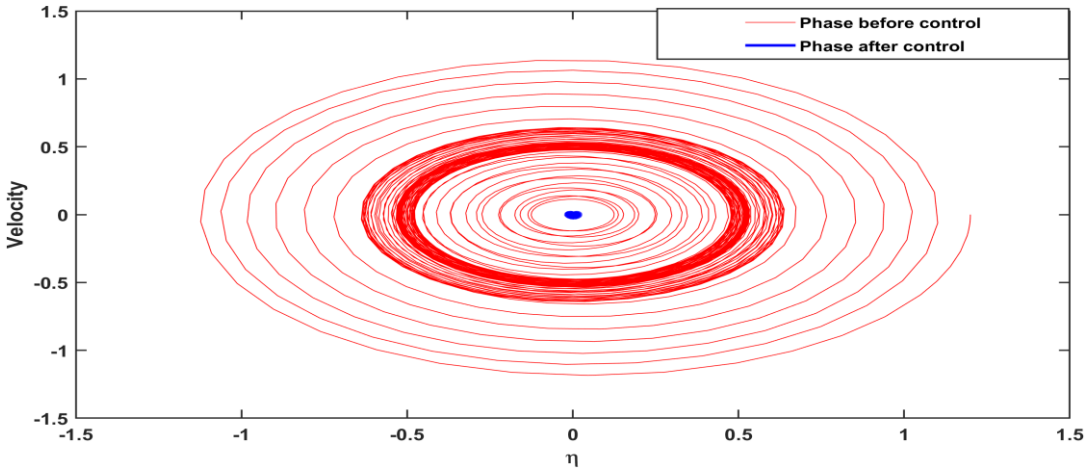

Figure 4. Comparison of phase portraits illustrating the system response before and after the application of control. The uncontrolled system exhibits large oscillatory trajectories, whereas the controlled system shows rapid convergence toward a stable equilibrium point, indicating effective vibration suppression.

3.4. Computational approach

Applying the Multiple Scale Perturbation technique (MSPT), as mentioned in [30,31], we get the perturbation solution for Eqs (2-a)–(2-c). The first approximation can be written in the following form:

$$\eta(t,\varepsilon)=\eta_0(T_0,T_1)+\varepsilon\eta_1(T_0,T_1)+O(\varepsilon^2), \tag{3-a}$$

$$v(t,\varepsilon)=v_0(T_0,T_1)+\varepsilon v_1(T_0,T_1)+O(\varepsilon^2), \tag{3-b}$$

$$z(t,\varepsilon)=z_0(T_0,T_1)+\varepsilon z_1(T_0,T_1)+O(\varepsilon^2), \tag{3-c}$$

where $T_0=t$,$T_1=\varepsilon t$, and $T_2=\varepsilon^2 t$. The derivatives will take the following type:

$$\frac{d}{dt}=D_0+\varepsilon D_1+..., \tag{4-a}$$

$$\frac{d^2}{dt^2}=D_0^2+2\varepsilon D_0D_1+..., \tag{4-b}$$

$$D_n=\frac{\partial}{\partial T_n}\ (n=0,1). \tag{4-c}$$

Equating components of like powers ε and applying Eqs (3) and (4) into (2) yields:

$O(\varepsilon^0)$

$$(D_0^2+\omega_1^2)\eta_0=0, \tag{5-a}$$

$$(D_0+\delta)v_0=-\alpha_3 D_0\eta_0, \tag{5-b}$$

$$(D_0^2+\omega_2^2)z_0=0. \tag{5-c}$$

$O(\varepsilon)$

$$\left.\begin{aligned}(D_0^2+\omega_1^2)\eta_1=&-2D_0D_1\eta_0-2\omega_1\xi_1D_0\eta_0-\beta\left(\eta_0(D_0\eta_0)^2+\eta_0^2D_0^2\eta_0\right)-\alpha_1\eta_0^3+\alpha_2 v_0\\&+f\cos(\Omega t)+\gamma_1 z_0,\end{aligned}\right\} \tag{6-a}$$

$$(D_0+\delta)v_1=-D_1v_0-\alpha_3(D_0\eta_1+D_1\eta_0), \tag{6-b}$$

$$(D_0^2+\omega_2^2)z_1=-2D_0D_1z_0-2\omega_2\xi_2D_0z_0+\gamma_2\eta_0. \tag{6-c}$$

Equations (5-a) through (5-c) have general responses that can be formally expressed as

$$\eta_0(T_0,T_1)=A_1(T_1)e^{i\omega_1T_0}+c.c., \tag{7-a}$$

$$v_0(T_0,T_1)=C(T_1)e^{-\delta T_0}-\frac{i\alpha_3\omega_1(\delta-i\omega_1)}{(\delta^2+\omega_1^2)}A_1(T_1)e^{i\omega_1T_0}+cc., \tag{7-b}$$

$$z_0=A_2(T_1)e^{i\omega_2T_0}+c.c, \tag{7-c}$$

where A_m $(m=1,2)$ is a complex function in T_1, and cc denotes complex conjugate functions of the surpassing idioms.

We derive the solutions of Eqs (6-a)–(6-c) as follows by substituting Eqs (7-a)–(7-c) into Eqs (6-a)–(6-c) and solving the resulting differential equations after removing the secular elements with the initial approach:

$$\left.\begin{aligned}(D_0^2+\omega_1^2)\eta_1=&\left[-2i\omega_1D_1A_1-2i\omega_1^2\xi_1A_1+(2\beta+3\alpha_1)\omega_1^2A_1^2\bar{A}_1-\frac{i\alpha_2\alpha_3\omega_1(\delta-i\omega_1)A_1}{(\delta^2+\omega_1^2)}\right]e^{i\omega_1T_0}\\&+\left[2\beta\omega_1^2A_1^3+\alpha_1\omega_1^2A_1^3\right]e^{3i\omega_1T_0}+\frac{f}{2}e^{i\Omega T_0}+[\gamma_1A_2]e^{i\omega_2T_0}+\alpha_2Ce^{-\delta T_0}+cc.,\end{aligned}\right\} \tag{8-a}$$

$$\left.\begin{aligned}(D_0+\delta)v_1=&\left[-D_1C+\frac{\delta\alpha_2\alpha_3C}{\delta^2+\omega_1^2}\right]e^{-\delta T_0}+\left[\frac{i\alpha_3\omega_1(\delta-i\omega_1)}{(\delta^2+\omega_1^2)}D_1A_1-\alpha_3D_1A_1\right]e^{i\omega_1T_0}\\&+\left[\frac{2i\omega_1\alpha_3\beta A_1^3+i\omega_1\alpha_1\alpha_3A_1^3}{8}\right]e^{3i\omega_1T_0}+cc.,\end{aligned}\right\} \tag{8-b}$$

$$(D_0^2+\omega_2^2)z_1=\left[-2i\omega_2D_1A_2-2i\omega_2^2\xi_2A_2\right]e^{i\omega_2T_0}+[\gamma_2A_1]e^{i\omega_1T_0}+cc. \tag{8-c}$$

The most typical answers to Eqs (8-a)–(8-c) are as follows:

$$\eta_1=\left[\frac{-2\beta A_1^3-\alpha_1A_1^3}{8}\right]e^{3i\omega_1T_0}+\left[\frac{\alpha_2C}{\delta^2+\omega_1^2}\right]e^{-\delta T_0}+cc., \tag{9-a}$$

$$\left.\begin{aligned}v_1=&\left[\frac{i\alpha_3\omega_1(\delta-i\omega_1)^2}{(\delta^2+\omega_1^2)^2}D_1A_1-\frac{\alpha_3(\delta-i\omega_1)}{(\delta^2+\omega_1^2)}D_1A_1\right]e^{i\omega_1T_0}\\&+\left[\frac{i\omega_1\alpha_3(2\beta+\alpha_1)(\delta-3i\omega_1)A_1^3}{8(\delta^2+9\omega_1^2)}\right]e^{3i\omega_1T_0}+cc.,\end{aligned}\right\} \tag{9-b}$$

$$C\left(T_1\right)=d\,e^{\left(\frac{\delta\alpha_2\alpha_3}{\delta^2+\omega_1^2}\right)T_1}, \tag{9-c}$$

$$z_1=0. \tag{9-d}$$

As shown in Figure 5, the system response is characterized by a single pronounced peak at the primary resonance condition ($\Omega\cong\omega_1$), while no evidence of higher-order resonance, such as third-order resonance, is observed. This indicates that the nonlinear interactions in this system do not lead to the activation of additional resonance branches within the considered parameter range.

Accordingly, the energy harvesting performance is mainly influenced by the primary resonance regime, which represents the most effective operating region for the system.

The following is a summary of the resonance scenarios from the equations:

Primary resonance: $\Omega\cong\omega_1$.

Internal resonance: $\omega_2\cong\omega_1$.

Simultaneous resonance: Any combination of the above resonance cases is considered simultaneous resonance.

We regarded the simultaneous resonance situation as one of these resonance examples: $\Omega\cong\omega_1$ and $\omega_2\cong\omega_1$ utilized with tiny detuning values as the resonance characteristics σ_1 and σ_2 according to:

$$\Omega\approx\omega_1+\varepsilon\sigma_1,\omega_2\approx\omega_1+\varepsilon\sigma_2. \tag{10}$$

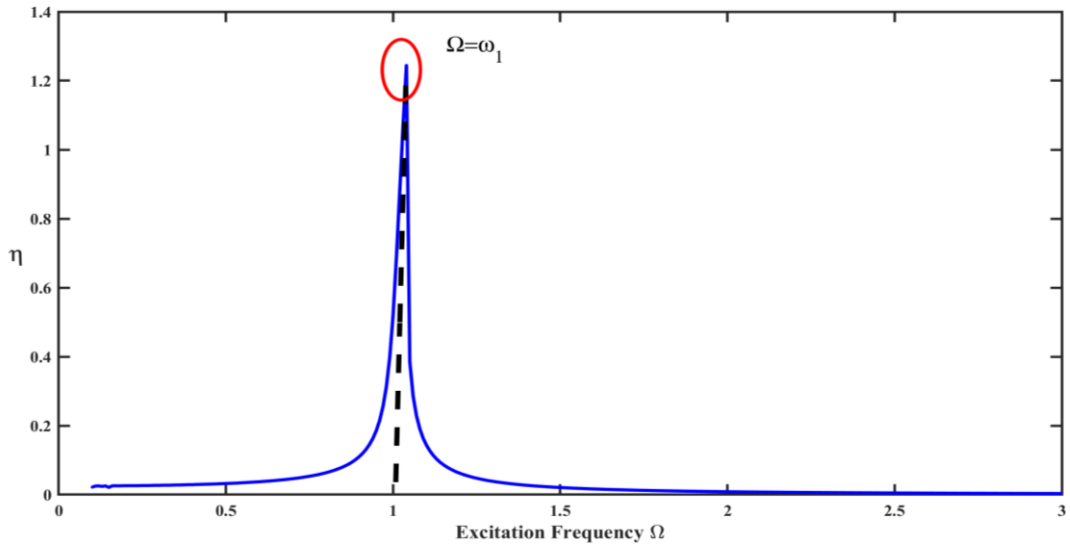

Figure 5. Frequency–response curve showing a dominant peak at the primary resonance ($\Omega\cong\omega_1$). No higher-order resonance peaks are observed, indicating that the system response is governed by the primary resonance under the parameters considered.

The solvency requirements are achieved by inserting Eq (10) into the relatively small divisor and

secular terms, which are derived using the first assumption in Eqs (8-a)–(8-c).

$$\left.\begin{aligned} 2i\omega_1 D_1 A_1 = &\left[-2i\omega_1^2\xi_1 A_1 + 2\omega_1^2\beta A_1^2\bar{A}_1 + 3\alpha_1\omega_1^2 A_1^2\bar{A}_1 - \frac{i\alpha_2\alpha_3\omega_1(\delta - i\omega_1)}{(\delta^2+\omega_1^2)}A_1\right] + \frac{f}{2}e^{i\sigma_1 T_1} \\ &+\left[\gamma_1 A_2\right]e^{i\sigma_2 T_1}, \end{aligned}\right\} \tag{11-a}$$

$$2i\omega_2 D_1 A_2 = \left[-2i\omega_2^2\xi_2 A_2\right] + \left[\gamma_2 A_1\right]e^{-i\sigma_2 T_1}. \tag{11-b}$$

In polar form, rephrase $A_n(T_1)$ as follows:

$$A_n(T_1) = \frac{1}{2}a_n(T_1)e^{i\chi_n(T_1)}, \tag{12}$$

where a_n are the steady-state amplitudes and χ_n are phases of the motion.
Combining the real and imaginary parts of Eqs (11-a)–(11-b) after entering Eq (12) results in

$$\dot{a}_1 = \left[-\omega_1\xi_1 a_1 - \frac{\alpha_2\alpha_3\delta}{2(\delta^2+\omega_1^2)}a_1\right] + \frac{f}{2\omega_1}\sin(\theta_1) + \left[\frac{\gamma_1}{2\omega_1}a_2\right]\sin(\theta_2), \tag{13-a}$$

$$a_1\dot{\chi}_1 = \left[-\frac{\omega_1\beta}{4}a_1^3 - \frac{3\alpha_1\omega_1}{8}a_1^3 + \frac{\alpha_2\alpha_3\omega_1}{2(\delta^2+\omega_1^2)}a_1\right] - \frac{f}{2\omega_1}\cos(\theta_1) - \left[\frac{\gamma_1}{2\omega_1}a_2\right]\cos(\theta_2), \tag{13-b}$$

$$\dot{a}_2 = \left[-\omega_2\xi_2 a_2\right] - \left[\frac{\gamma_2}{2\omega_2}a_1\right]\sin(\theta_2), \tag{13-c}$$

$$a_2\dot{\chi}_2 = -\left[\frac{\gamma_2}{2\omega_2}a_1\right]\cos(\theta_2), \tag{13-d}$$

where $\theta_1 = (\Omega - \omega_1)T_1 - \chi_1, \theta_2 = (\omega_2 - \omega_1)T_1 + \chi_2 - \chi_1$.

Then we get $\dot{\chi}_1 = (\Omega - \omega_1) - \dot{\theta}_1$ and $\dot{\chi}_2 = \dot{\theta}_2 - \dot{\theta}_1 + (\Omega - \omega_2)$. By inserting the final derivative solutions into Eqs (12-a) and (12-d), we obtain:

$$\dot{\theta}_1 = \left[(\Omega - \omega_1) + \frac{\omega_1\beta}{4}a_1^2 + \frac{3\alpha_1\omega_1}{8}a_1^2 - \frac{\alpha_2\alpha_3\omega_1}{2(\delta^2+\omega_1^2)}\right] + \frac{f}{2\omega_1 a_1}\cos(\theta_1) + \left[\frac{\gamma_1}{2\omega_1 a_1}a_2\right]\cos(\theta_2), \tag{14-a}$$

$$\dot{\theta}_2 = \dot{\theta}_1 - (\Omega - \omega_2) - \left[\frac{\gamma_2}{2\omega_2 a_2}a_1\right]\cos(\theta_2). \tag{14-b}$$

3.5. Frequency response equations

The building components are the focus of an examination $\dot{a}_m = 0, \dot{\theta}_m = 0$. The frequency response equations that are displayed next are developed using stable solutions and periodic solutions at the fixed points in Eqs (12-a)–(12-c):

$$0 = \left[-\omega_1 \xi_1 a_1 - \frac{\alpha_2 \alpha_3 \delta}{2\left(\delta^2 + \omega_1^2\right)} a_1 \right] + \frac{f}{2\omega_1} \sin\left(\theta_1\right) + \left[\frac{\gamma_1}{2\omega_1} a_2 \right] \sin\left(\theta_2\right), \tag{15-a}$$

$$a_1\left(\Omega - \omega_1\right) = \left[-\frac{\omega_1 \beta}{4} a_1^3 - \frac{3\alpha_1 \omega_1}{8} a_1^3 + \frac{\alpha_2 \alpha_3 \omega_1}{2\left(\delta^2 + \omega_1^2\right)} a_1 \right] - \frac{f}{2\omega_1} \cos\left(\theta_1\right) - \left[\frac{\gamma_1}{2\omega_1} a_2 \right] \cos\left(\theta_2\right), \tag{15-b}$$

$$0 = \left[-\omega_2 \xi_2 a_2 \right] - \left[\frac{\gamma_2}{2\omega_2} a_1 \right] \sin\left(\theta_2\right), \tag{15-c}$$

$$a_2\left(\Omega - \omega_2\right) = -\left[\frac{\gamma_2}{2\omega_2} a_1 \right] \cos\left(\theta_2\right). \tag{15-d}$$

Equations (15-c) and (15-d) give us:

$$\sin\left(\theta_2\right) = \left[-\frac{2\omega_2^2 \xi_2 a_2}{\gamma_2 a_1} \right], \tag{16-a}$$

$$\cos\left(\theta_2\right) = \left[-\frac{2\omega_2 a_2 \left(\Omega - \omega_2\right)}{\gamma_2 a_1} \right]. \tag{16-b}$$

Equations (16-a) and (16-b) can be substituted into (15-a) and (15-b) to obtain:

$$\sin\left(\theta_1\right) = \left[\frac{2\omega_1}{f} \right] \left[\omega_1 \xi_1 a_1 + \frac{\alpha_2 \alpha_3 \delta}{2\left(\delta^2 + \omega_1^2\right)} a_1 + \frac{\gamma_1 \omega_2^2 \xi_2 a_2^2}{\omega_1 \gamma_2 a_1} \right], \tag{17-a}$$

$$\cos\left(\theta_1\right) = \left[\frac{2\omega_1}{f} \right] \left[-a_1\left(\Omega - \omega_1\right) - \frac{\omega_1 \beta}{4} a_1^3 - \frac{3\alpha_1 \omega_1}{8} a_1^3 + \frac{\alpha_2 \alpha_3 \omega_1}{2\left(\delta^2 + \omega_1^2\right)} a_1 + \frac{\gamma_1 \omega_2 a_2^2 \left(\Omega - \omega_2\right)}{\omega_1 \gamma_2 a_1} \right]. \tag{17-b}$$

Next, by squaring and adding each side of Eqs (17-a) and (17-b), the frequency response equations can be expressed as follows:

$$\left(\omega_1\xi_1 a_1+\frac{\alpha_2\alpha_3\delta}{2\left(\delta^2+\omega_1^2\right)}a_1+\frac{\gamma_1\omega_2^2\xi_2 a_2^2}{\omega_1\gamma_2 a_1}\right)^2+\left(\begin{array}{l}-a_1\left(\Omega-\omega_1\right)-\dfrac{\omega_1\beta}{4}a_1^3-\dfrac{3\alpha_1\omega_1}{8}a_1^3\\+\dfrac{\alpha_2\alpha_3\omega_1}{2\left(\delta^2+\omega_1^2\right)}a_1+\dfrac{\gamma_1\omega_2 a_2^2\left(\Omega-\omega_2\right)}{\omega_1\gamma_2 a_1}\end{array}\right)^2=\left[\frac{f^2}{4\omega_1^2}\right],\tag{18-a}$$

$$a_1^2=\left[\frac{4\omega_2^4\xi_2^2+4\omega_2^2\left(\Omega-\omega_2\right)^2}{\gamma_2^2}\right]a_2^2.\tag{18-b}$$

3.6. Stability of the problem

To determine whether the nonlinear solution of the obtained fixed points is stable, let the following

$$a_m=a_{m0}+a_{m1},\theta_m=\theta_{m0}+\theta_{m1},\tag{19}$$

where a_{m0} and θ_{m0} are solutions of Eqs (13) and (14), and a_{m1}, θ_{m1} are small perturbations, which are thought to be minimal when compared to a_{m0} and θ_{m0}.

The framework of first-order differential equations might be expressed in the matrix that follows form by substituting Eq (19) into (13-a)–(13-d) and expanding for small $a_{11},a_{21},\theta_{11},\theta_{21}$ to carry on linear terms only:

$$\left.\begin{aligned}\dot{a}_{11}=&\left[-\omega_1\xi_1-\frac{\alpha_2\alpha_3\delta}{2\left(\delta^2+\omega_1^2\right)}\right]a_{11}+\left[\frac{f}{2\omega_1}\cos\left(\theta_{10}\right)\right]\theta_{11}+\left[\frac{\gamma_1}{2\omega_1}\sin\left(\theta_{20}\right)\right]a_{21}\\&+\left[\frac{\gamma_1}{2\omega_1}a_{20}\cos\left(\theta_{20}\right)\right]\theta_{21},\end{aligned}\right\}\tag{20-a}$$

$$\left.\begin{aligned}\dot{\theta}_{11}=&\left[\frac{\left(\Omega-\omega_1\right)}{a_{10}}+\frac{3\omega_1\beta}{4}a_{10}+\frac{9\alpha_1\omega_1}{8}a_{10}-\frac{\alpha_2\alpha_3\omega_1}{2a_{10}\left(\delta^2+\omega_1^2\right)}\right]a_{11}+\left[-\frac{f}{2a_{10}\omega_1}\sin\left(\theta_{10}\right)\right]\theta_{11}\\&+\left[\frac{\gamma_1}{2a_{10}\omega_1}\cos\left(\theta_{20}\right)\right]a_{21}+\left[-\frac{\gamma_1}{2\omega_1 a_{10}}a_{20}\sin\left(\theta_{20}\right)\right]\theta_{21},\end{aligned}\right\}\tag{20-b}$$

$$\dot{a}_{21}=\left[-\frac{\gamma_2}{2\omega_2}\sin\left(\theta_{20}\right)\right]a_{11}+\left[-\omega_2\xi_2\right]a_{21}+\left[-\frac{\gamma_2}{2\omega_2}a_{10}\cos\left(\theta_{20}\right)\right]\theta_{21},\tag{20-c}$$

$$\dot{\theta}_{21}=\left[\frac{(\omega_2-\omega_1)}{a_{10}}+\frac{3\omega_1\beta}{4}a_{10}+\frac{9\alpha_1\omega_1}{8}a_{10}-\frac{\alpha_2\alpha_3\omega_1}{2\left(\delta^2+\omega_1^2\right)a_{10}}-\frac{\gamma_2}{\omega_2 a_{20}}\cos(\theta_{20})\right]a_{11}$$
$$+\left[\frac{-f}{2a_{10}\omega_1}\sin(\theta_{10})\right]\theta_{11}+\left[\begin{array}{l}\frac{(\omega_2-\omega_1)}{a_{20}}+\frac{\omega_1\beta}{4a_{20}}a_{10}^2+\frac{3\alpha_1\omega_1}{8a_{20}}a_{10}^2-\frac{\alpha_2\alpha_3\omega_1}{2\left(\delta^2+\omega_1^2\right)a_{20}}\\+\frac{f}{2\omega_1 a_{10}a_{20}}\cos(\theta_{10})+\frac{\gamma_1}{\omega_1 a_{10}}\cos(\theta_{20})\end{array}\right]a_{21}\Bigg\}$$
$$+\left[-\left(\frac{\gamma_1}{2\omega_1 a_{10}}a_{20}-\frac{\gamma_2}{2\omega_2 a_{20}}a_{10}\right)\sin(\theta_{20})\right]\theta_{21}. \tag{20-d}$$

The algebraic equation's shape is found in the next matrix

$$\left[\dot{a}_{11}\quad\dot{\theta}_{11}\quad\dot{a}_{21}\quad\dot{\theta}_{21}\right]^T=[J]\left[a_{11}\quad\theta_{11}\quad a_{21}\quad\theta_{21}\right]^T. \tag{21}$$

The Jacobian matrix J can be defined using the right portions of Eq (21) as:

$$[J]=\begin{bmatrix}M_{11}&M_{12}&M_{13}&M_{14}\\M_{21}&M_{22}&M_{23}&M_{24}\\M_{31}&M_{32}&M_{33}&M_{34}\\M_{41}&M_{42}&M_{43}&M_{44}\end{bmatrix}, \tag{22}$$

where $[J]$ is the Jacobian matrix and $M_{ij}\,(i=1,2,3,4)(j=1,2,3,4)$ are defined in the Appendix.

Equation (22) is placed in the following determinant form to get the eigenvalues of the 4×4 preceding Jacobian matrix:

$$\begin{vmatrix}M_{11}-\lambda&M_{12}&M_{13}&M_{14}\\M_{21}&M_{22}-\lambda&M_{23}&M_{24}\\M_{31}&M_{32}&M_{33}-\lambda&M_{34}\\M_{41}&M_{42}&M_{43}&M_{44}-\lambda\end{vmatrix}=0. \tag{23}$$

As a result, we set out to determine the roots of a characteristic polynomial problem and solve the determinant of which identified polynomial has the roots listed below

$$\lambda^4+\Gamma_1\lambda^3+\Gamma_2\lambda^2+\Gamma_3\lambda+\Gamma_4=0, \tag{24}$$

where Γ_i are functions into M_{ij}.

The related equilibrium solution is asymptotically stable if the real part of each eigenvalue is negative; otherwise, it grows unstable. The Routh-Hurwitz criterion states that if just the determinant D and all of its primary minors are positive, then the necessary and sufficient conditions for all of the roots of Eq (24)

have negative real parts.

$$D = \begin{vmatrix} \Gamma_1 & 1 & 0 & 0 \\ \Gamma_3 & \Gamma_2 & \Gamma_1 & 1 \\ 0 & \Gamma_4 & \Gamma_3 & \Gamma_2 \\ 0 & 0 & 0 & \Gamma_4 \end{vmatrix}. \tag{25}$$

4. Remarks and feedback

4.1. Impacts of the parameters

The impacts of different coefficients in the PPF-controlled model are depicted in detail by the FRC, which is displayed in Figures 6–16. Interestingly, several of the parameters have stable and unstable areas when their values change, while the curves occasionally show only stable regions with no unstable sectors. Furthermore, the stability setting has two unique peaks.

First, let us illustrate Figure 6, which gives a smooth U-shaped variation of the response amplitude a_1 as a function of the excitation frequency ratio Ω. The curve shows a minimum amplitude near $\Omega = 1$, indicating a point of optimal dynamic behavior where the system experiences the least vibration. As Ω deviates from this optimal point in either direction, the amplitude increases symmetrically, reflecting the frequency sensitivity of the system. The response amplitude a_1 change regarding the detuning parameter σ_1 is plotted in Figure 7. Strong nonlinear resonance behavior is indicated by two conspicuous resonance peaks that appear close to $\sigma_1 = -10$ and $\sigma_1 = 10$, where the amplitude increases dramatically. The amplitude smoothly decreases toward low values away from these resonant locations, indicating a steady off-resonance response. The dispersed points surrounding the peaks allude to multi-valued solutions or numerical sensitivity, which are frequently connected to nonlinear systems. Overall, the curve shows how a_1 strongly depends on the detuning parameter and exhibits symmetric resonance behavior. The response curves in Figure 8 show noticeable variations in the stable (red) and unstable (blue) branches as the nonlinear stiffness parameter β grows. Increased amplitude levels, sharper resonance peaks, and more pronounced solution curve bending result from higher values of β, intensifying the nonlinear effects. Wider areas where several solutions coexist are produced as a result, with the stable red branches getting more warped and the unstable blue branches growing. In general, raising β increases the complexity of the frequency-response structure and reinforces the system's nonlinear behavior. The response surfaces show a distinct nonlinear fluctuation in both a and b as the excitation frequency *f* increases, as in Figure 9. The stable (red) branches exhibit a smooth trend, and the amplitudes stay minimal for low values of *f*. The system experiences a discernible increase in amplitude as *f* keeps rising, which causes the stable curves to bend upward and take on the distinctive nonlinear backbone shape.

Moreover, the unstable (blue) branches appear between the stable segments, typically around the resonance region. These unstable segments expand or contract depending on the value of *f*, marking the transition between low- and high-amplitude stable solutions. Overall, increasing *f* shifts the system from low-amplitude behavior to higher-amplitude nonlinear responses, revealing the typical multivalued structure associated with nonlinear resonance. Moreover, between the stable segments, usually in the vicinity of the resonance region, appear the unstable (blue) branches. Depending on the

value of *f*, these unstable segments grow or decrease, signifying the change from low-amplitude to high-amplitude stable solutions. All things considered, raising *f* causes the system to transition from low-amplitude behavior to higher-amplitude nonlinear responses, exposing the characteristic multivalued structure linked to nonlinear resonance. The two three-dimensional figures in Figure 10 illustrate how the detuning parameter σ_1 and the cubic stiffness parameter α_1 affect the modal amplitudes *a* (left) and *b* (right). The system's nonlinear features become more noticeable as α_1 rises, resulting in sharper resonance peaks and distinct bending of the stable solution branches (red). The regions of multivalued response are indicated by the unstable branches (blue), which stay limited close to low amplitudes. Overall, the figures show that α_1 has a significant impact on the nonlinear resonance responses' strength, shifting, and form for both amplitudes. The two three-dimensional figures show how the modal amplitudes *a* (left) and *b* (right) change as a function of the internal frequency parameter ω_1 and the detuning parameter σ_1. Figure 11 illustrates how the system amplitudes *a* (left) and *b* (right) vary simultaneously with respect to parameters σ_1 and α_2. The red curves depict the response surfaces, revealing a sequence of sharp resonance peaks that shift in magnitude and location as the parameters change. Increasing α_2 tends to move the resonance ridges across the σ_1–axis, while the amplitude levels differ significantly between a and b, indicating their different sensitivities to the same parametric variations. The overall structure highlights strong nonlinear behavior, with multiple localized peaks and steep gradients across the parameter domain. The resonance peaks shift and spread out as ω_1 grows, demonstrating how changes in internal frequency have a significant impact on the nonlinear response of the system. The curves show several resonance locations, with sharp amplitude growth close to particular σ_1 and combinations. Overall, the plot shows how the nonlinear resonance structure is reshaped by internal frequency fluctuations and emphasizes how sensitive both amplitudes are to frequency interactions, as shown in Figure 12. The steady-state amplitudes *a* (left) and *b* (right) are plotted in three dimensions as functions of the damping ratio ξ_2 and the detuning parameter σ_1 in Figure 13. A series of prominent resonance peaks can be seen in the red response curves; these peaks' positions and magnitudes vary considerably with changes in ξ_2. The resonance ridges shift and peak amplitudes often fall as ξ_2 increases, suggesting increased damping and less vibratory responsiveness. Comparing the two subfigures reveals that amplitude *a* is more sensitive to changes in the same parameter, as evidenced by its greater peak values and more noticeable nonlinear behavior. Overall, the graphic shows how damping is essential in determining the system's resonance structure.

Figure 14 shows the response of amplitudes *a* (left) and *b* (right) in the 3D plots as functions of the stiffness-related parameter σ_1 and the detuning parameter δ. The related unstable branches are indicated by blue curves, while the stable steady-state branches are represented by red curves with distinct resonance peaks that shift and change magnitude with changes in δ. The resonance peaks shrink and become more sensitive to detuning as σ_1 drops toward more negative values, while the response swings toward higher δ with more noticeable multi-peak behavior when σ_1 increases. Overall, the surfaces show distinct transitions between stable and unstable regimes and emphasize the system's oscillation amplitudes' substantial nonlinear reliance on both parameters.

The graphics show how the stiffness parameter σ_1 and the coupling parameter γ_1 affect the system's three-dimensional dynamic response. In Figure 15, the fundamental amplitude *a* creates many nonlinear resonance branches in panel (a). Solid red curves represent stable steady-state solutions, whereas blue curves show unstable behavior. The height and position of these peaks fluctuate

significantly when γ_1 varies, indicating how strongly the principal response depends on the combined influence of coupling and stiffness. The equivalent evolution of the secondary amplitude b is displayed in panel (b). The unstable parts show up as wavering blue solid line arcs, whereas the stable branches climb sharply close to resonance. The redistribution of energy between the two modes is reflected in the movement of these peaks when γ_1 changes. Overall, the plots show that there are several resonance paths and emphasize the intricate nonlinear link between dynamic performance and system characteristics. In Figure 16, response surfaces of the system with respect to the coupling parameter γ_2 and the principal stiffness parameter σ_1 are depicted in the images. The amplitude in panel (a) shows steeply peaked branches (solid red) that correspond to stable solutions, while the accompanying unstable responses are represented by blue curves. The solution structure shows several resonance-like peaks that change in location and size as γ_2 fluctuates, suggesting that the principal response is highly sensitive to the combined effects of coupling and stiffness. The evolution of the secondary amplitude in panel (b) has a similar pattern: Unstable branches show up as oscillating blue solid segments, whereas stable branches form smooth, sharply increasing response curves. The branches move outward and change slope as γ_2 grows, demonstrating how the linked system redistributes energy between the two coordinates. Overall, the figures amply illustrate how parameters interact nonlinearly and how different stable and unstable regimes occur throughout the parameter space under investigation.

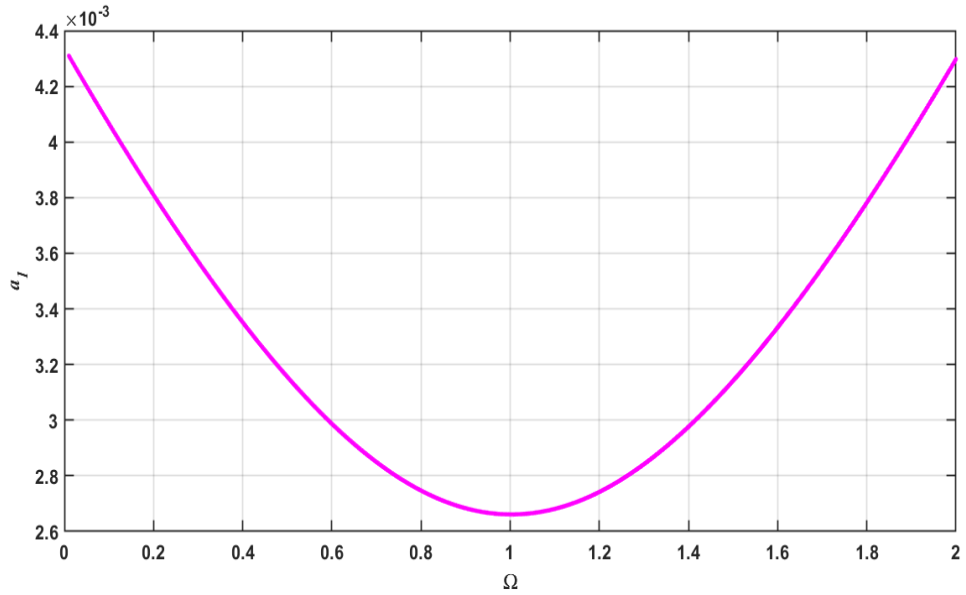

Figure 6. Variation of the primary response amplitude a_1 with the excitation frequency ratio Ω.

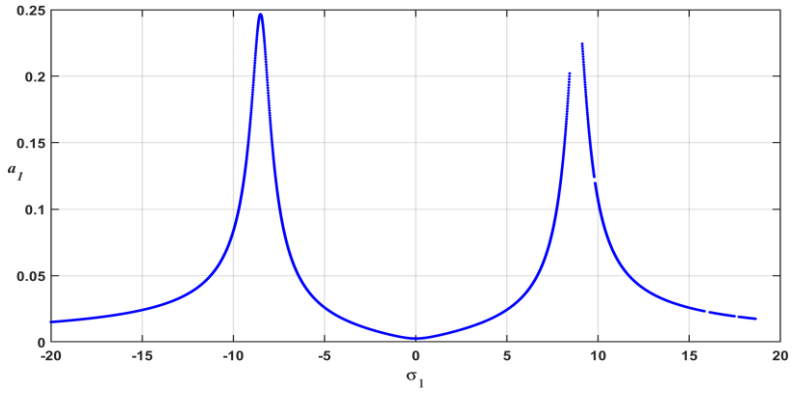

Figure 7. Frequency response curves at the detuning parameter σ_1, showing the variation of the steady-state amplitude a_1. The figure illustrates the nonlinear resonance characteristics of the system.

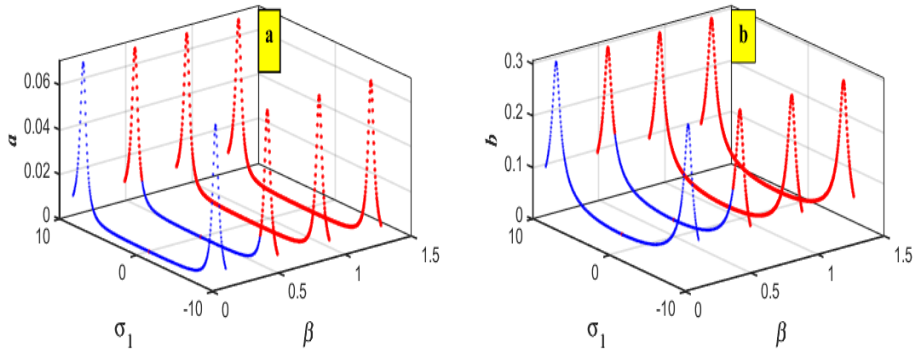

Figure 8. The frequency response path of the nonlinear vibrations on the PEH is obtained at different values when the control is implemented with β. (a) A case study of the reaction of β via *a*. (b) A case study of the reaction of β via *b*. The blue line refelects the unstable effect and the red solid lines reflect the stable curve.

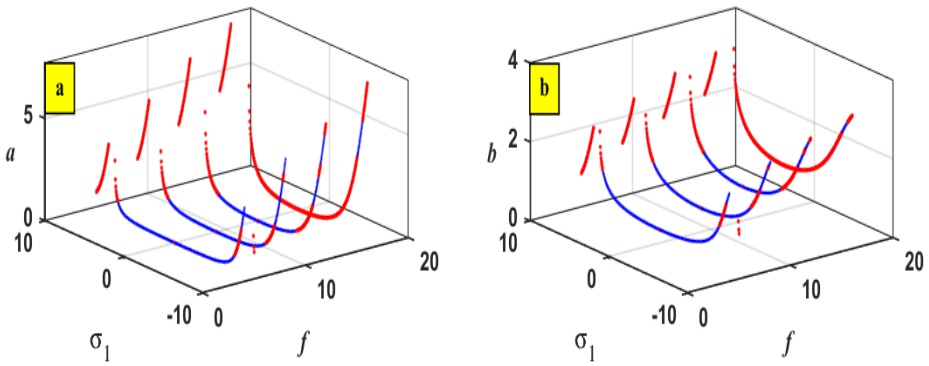

Figure 9. The frequency response path of the nonlinear vibrations on the PEH is obtained at different values when the control is implemented with f. (a) A case study of the reaction of f via a. (b) A case study of the reaction of f via b. The blue line reflects the unstable effect and the red solid lines reflect the stable curve.

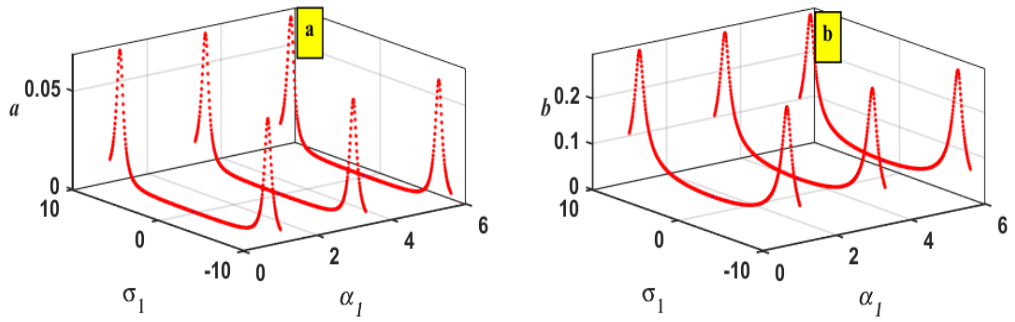

Figure 10. The frequency response path of the nonlinear vibrations on the PEH is obtained at different values when the control is implemented with α_1. (a) A case study of the reaction of α_1 via *a*. (b) A case study of the reaction of α_1 via *b*.

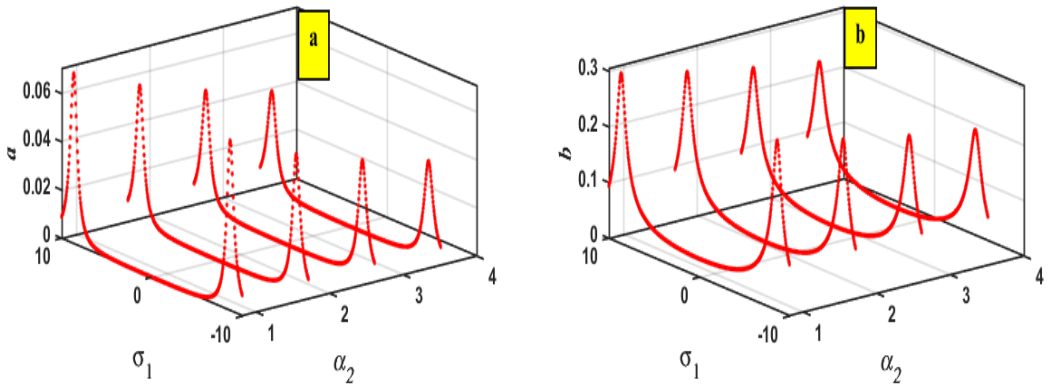

Figure 11. The frequency response path of the nonlinear vibrations on the PEH is obtained at different values when the control is implemented with α_2. (a) A case study of the reaction of α_2 via *a*. (b) A case study of the reaction of α_2 via *b*.

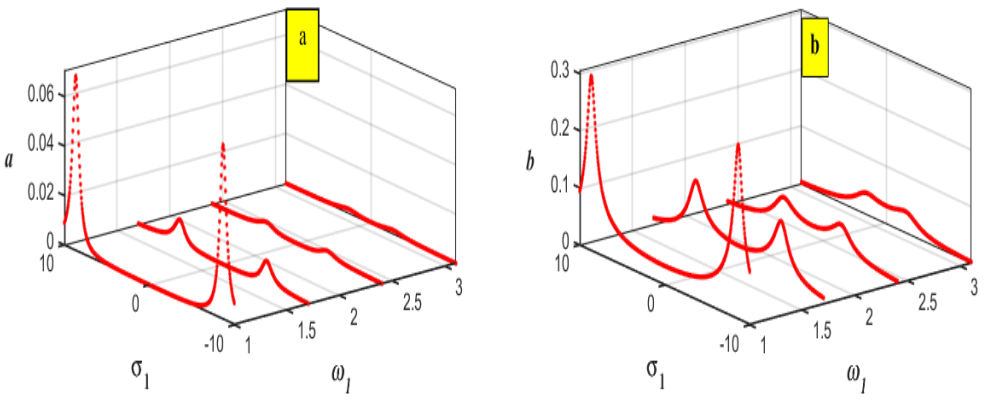

Figure 12. The frequency response path of the nonlinear vibrations on the PEH is obtained at different values when the control is implemented with ω_1. (a) A case study of the reaction of ω_1 via *a*. (b) A case study of the reaction of ω_1 via *b*.

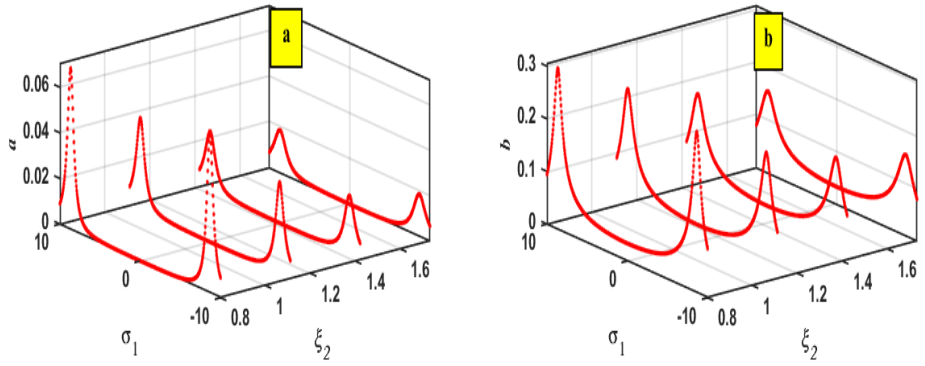

Figure 13. The frequency response path of the nonlinear vibrations on the PEH is obtained at different values when the control is implemented with ξ_2. (a) A case study of the reaction of ξ_2 via *a*. (b) A case study of the reaction of ξ_2 via *b*.

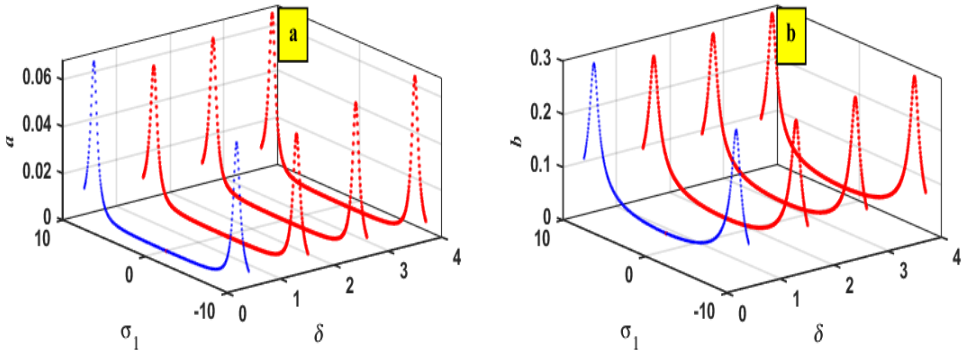

Figure 14. The frequency response path of the nonlinear vibrations on the PEH is obtained at different values when the control is implemented with δ. (a) A case study of the reaction of δ via *a*. (b) A case study of the reaction of δ via *b*. The blue line reflects the unstable effect and the red solid lines reflect the stable curve.

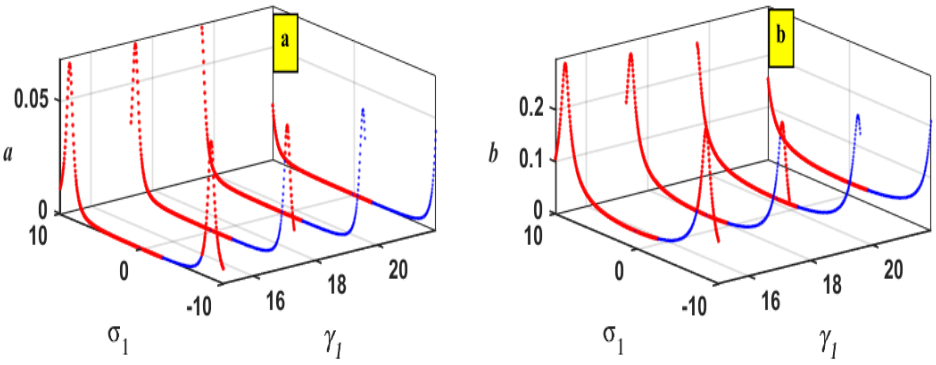

Figure 15. The frequency response path of the nonlinear vibrations on the PEH is obtained at different values when the control is implemented with γ_1. (a) A case study of the reaction of γ_1 via *a*. (b) A case study of the reaction of γ_1 via *b* .The blue line reflects the unstable effect and the red solid lines reflect the stable curve.

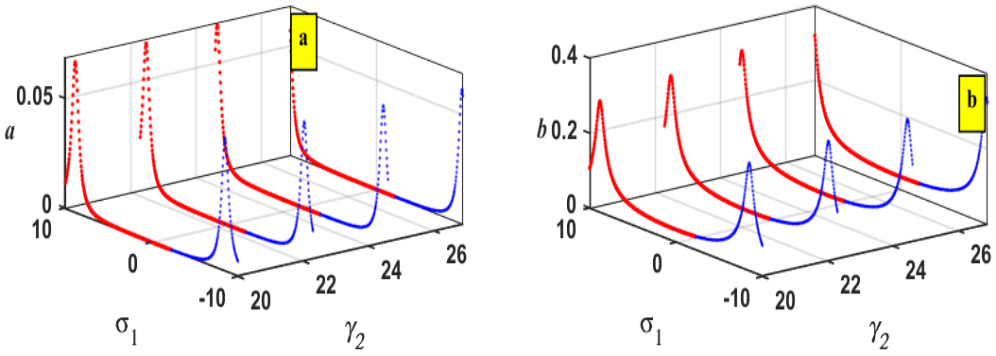

Figure 16. The frequency response path of the nonlinear vibrations on the PEH is obtained at different values when the control is implemented with γ_2. (a) A case study of the reaction of γ_2 via a. (b) A case study of the reaction of γ_2 via b. The blue line reflects the unstable effect and the red solid lines reflect the stable curve.

4.2. A graph comparing the MTSM inquiry and numerical simulation

Two comparison graphs are included in this part to highlight our goal of the study.

Figure 17 compares the analytically obtained frequency-response curve (solid cyan line) with the numerical results generated using the Runge–Kutta method (red markers). The two datasets exhibit excellent agreement over the range of the detuning parameter, particularly near the resonance regions, where the response amplitude increases significantly. The close overlap between the analytical predictions and numerical results confirms the accuracy of the developed mathematical model and demonstrates that the Runge–Kutta method effectively captures the nonlinear dynamic behavior of the system.

A slight discrepancy between the analytical and numerical results can be observed in Figure 17. This deviation is mainly attributed to the truncation of higher-order terms in the MSPT, as well as minor numerical effects related to the time-stepping scheme and solver tolerances used in MATLAB. Nevertheless, the overall agreement remains excellent, confirming the accuracy of the proposed approach.

In Figure 18, the time-history responses amply illustrate how well the Positive Position Feedback (PPF) controller suppresses vibrations in both displacement η (Figure 18(a)) and the second part of the system v (Figure 18(b)). The system shows persistent oscillations with comparatively large amplitudes before the application of control, suggesting weak intrinsic damping. The responses quickly fade toward zero after the PPF controller is turned on, and the steady-state oscillations are almost gone. The controller's strong capacity to improve damping and stabilize the system, resulting in quick vibration attenuation and noticeably smoother long-term behavior, is shown by the stark difference between the uncontrolled (cyan/yellow) and controlled (green/magenta) signals.

It is important to note that, in piezoelectric energy harvesting systems, the electrical output is directly coupled to the mechanical response. Since the generated voltage is proportional to displacement η. Moreover, significant reduction in oscillation amplitude and suppression of nonlinear phenomena observed in Figure 16 indicate a corresponding improvement in the stability and effectiveness of the harvested electrical signal.

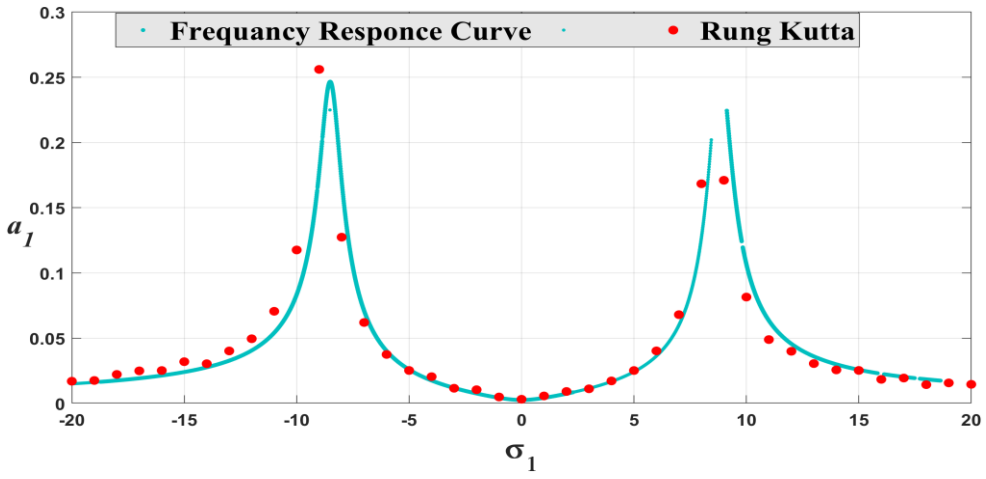

Figure 17. 2-DOF PEH oscillation of a_1 against σ_1 when $f = 0.5$. The solid line refers to a stable periodic solution, and the red circles are from a numerical simulation.

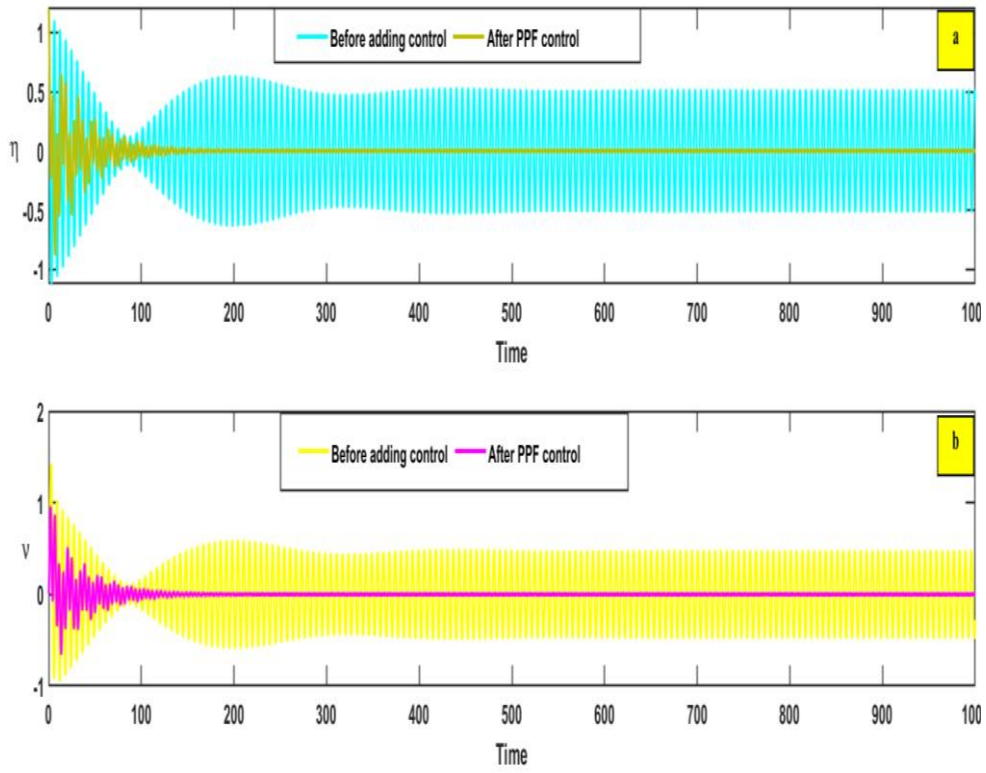

Figure 18. Comparison of the system response before and after applying PPF control. The uncontrolled system exhibits large-amplitude oscillations and nonlinear jump phenomena, whereas the controlled system shows significantly reduced vibrations and faster convergence to a steady state. This is due to the inherent electromechanical coupling in piezoelectric systems, where the generated voltage is proportional to structural displacement ($V(t) \propto \eta(t)$). The improved dynamic behavior directly implies a more stable and effective electrical output.

5. Bifurcation classification

In this portion of the study, understanding the complexity of structures with nonlinear dynamics requires investigating unanticipated activities. As we see in this instance, the system goes through transitions anytime its parameters change. These changes may lead to a wide spectrum of behavior, from chaos to regular cyclical movement. These changes are succinctly summarized using bifurcation visualization, which highlights the evolution of the mechanism as a critical variable. The modified mechanism has been assessed using MATLAB; phase portraits and bifurcation charts are also shown in the results.

The bifurcation diagram in Figure 19 reveals a sequence of qualitative transitions in the system's response as excitation frequency Ω varies. Although the amplitude–frequency curve may initially suggest the presence of chaotic motion, a detailed inspection using the Poincaré map and phase portrait indicates otherwise. For low values of Ω ($\Omega \approx 0 \to 0.8$), the phase trajectories form nested closed curves and the Poincaré sections lie on smooth invariant loops, confirming that the response is quasi-periodic rather than chaotic. As Ω increases, the system collapses onto a single closed orbit, and the Poincaré section reduces to a discrete set of points, indicating a transition to a periodic solution. This periodic window persists over a finite frequency range. Beyond this region, the system again exhibits invariant loops in the Poincaré map and multi-loop trajectories in phase space, demonstrating a return to quasi-periodic motion. Importantly, at no stage do the Poincaré points scatter to fill an area, and no sensitive dependence is observed in the phase portrait, indicating the absence of chaos in the investigated frequency range.

The bifurcation diagram presented in Figure 19 reveals that the system dynamics are confined to periodic and quasi-periodic motions within the investigated parameter ranges, with no indication of chaotic behavior. This observation is further supported by the corresponding phase portraits shown in Figure 17(a)–(c). Specifically, Figure 19(a,b) display well-defined closed trajectories, confirming stable limit cycle oscillations, whereas Figure 19(c) exhibits multiple nested closed orbits, indicating quasi-periodic motion evolving on a toroidal manifold. The absence of irregular, scattered, or fractal-like structures in the bifurcation diagram and phase space confirms that chaotic attractors do not arise in this system.

Figure 20 shows the system's dynamic response through phase portraits (blue) and Poincaré sections (red) at three representative excitation frequencies. Figure 20(a) $\Omega = 0.8$: Quasi-periodic motion; trajectories form invariant closed loops and the Poincaré points lie on smooth curves. Figure 20(b) $\Omega = 2$: Periodic motion; the response collapses onto a single limit cycle and the Poincaré section reduces to a discrete set of points (period-1). Figure 20(c) $\Omega = 4$: Quasi-periodic motion; multi-loop invariant curves reappear. These observations are consistent with the bifurcation diagram, which shows quasi-periodic behavior at low and high Ω with a periodic window around $\Omega \approx 4$, confirming the absence of chaotic dynamics in the studied frequency range.

From an energy harvesting perspective, such regular dynamic responses are highly desirable, as periodic and quasi-periodic oscillations provide stable and predictable mechanical inputs to the piezoelectric element. In contrast, although chaotic motion, if present, may introduce broadband frequency content that can enhance instantaneous energy extraction, it typically leads to fluctuating and less reliable power output. Therefore, the suppression of complex nonlinear behavior and the promotion of regular oscillations, particularly through the implementation of the PPF controller, contribute significantly to improving the stability and effectiveness of the energy harvesting process.

No chaotic motion is observed within the investigated parameter range.

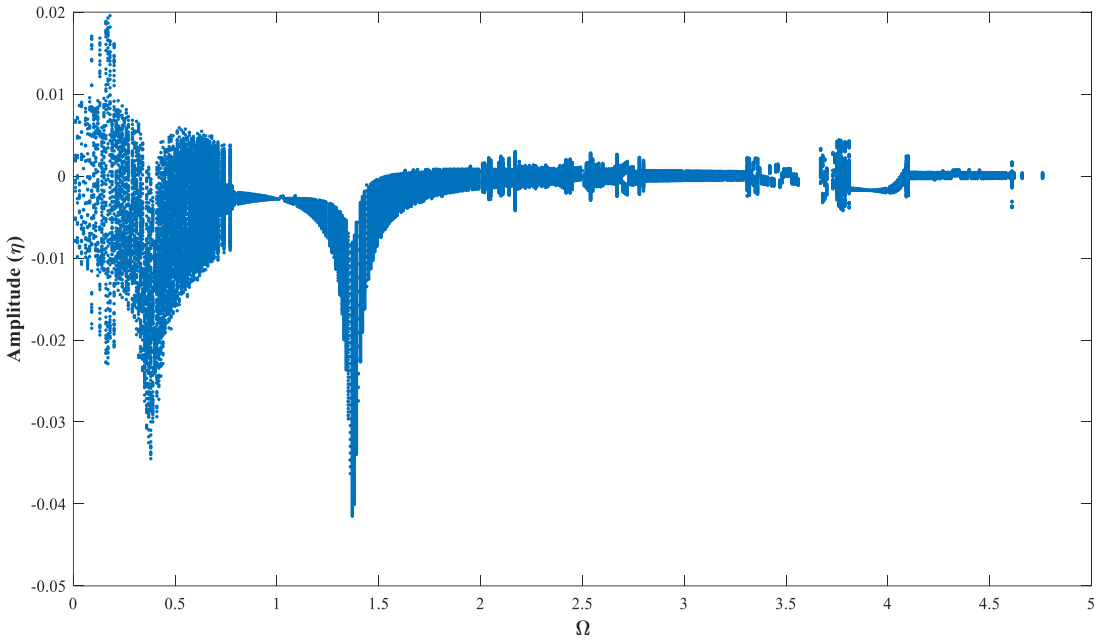

Figure 19. Diagrams of bifurcation η of opposing Ω.

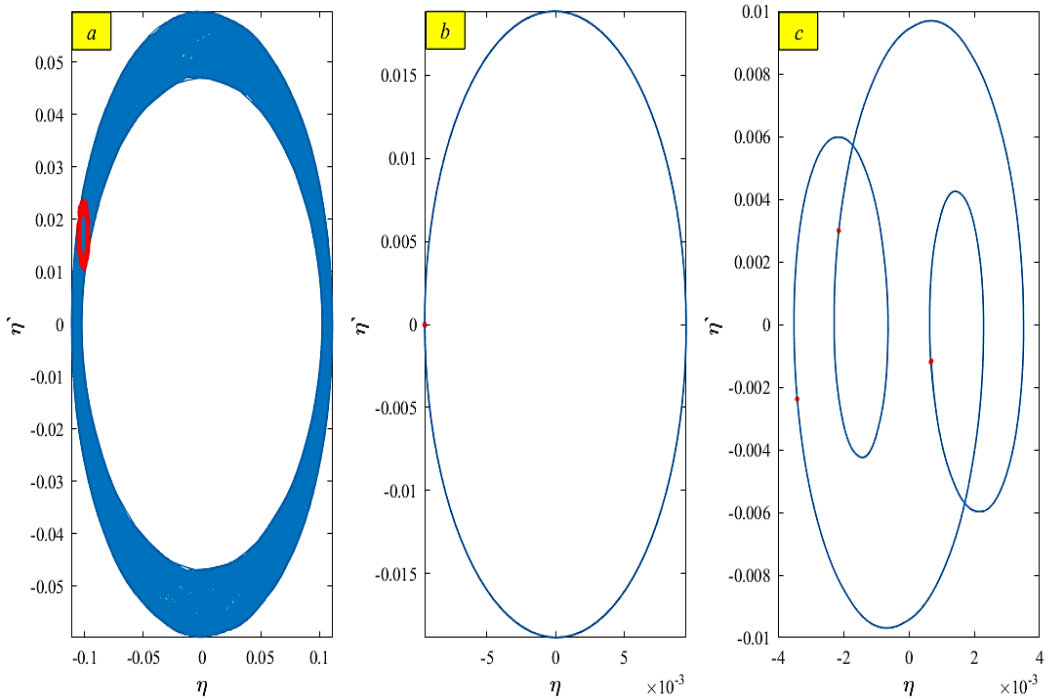

Figure 20. Poincaré diagrams and phase portraits for the parameters that are quasi-periodic for η and η'.

6. Conclusions

In this study, we present a comprehensive analytical–numerical investigation of the nonlinear dynamics of a broadband piezoelectric energy harvester (PEH) subjected to simultaneous primary and internal resonances. The second-order MSPT is employed to derive accurate analytical solutions, which are validated through numerical simulations performed using MATLAB and MAPLE, showing excellent agreement in frequency-response curves, time histories, and phase portraits. A unified framework incorporating PPF control is developed to examine its influence on system behavior. The results demonstrate that the proposed controller effectively suppresses vibration amplitudes, mitigates nonlinear jump phenomena, and significantly reduces settling time compared to the uncontrolled system. Bifurcation analysis reveals the existence of periodic and quasi-periodic responses, with no evidence of chaotic dynamics within the investigated parameter range. Stability is rigorously assessed using the Routh–Hurwitz criterion applied to the Jacobian system, while parametric studies highlight the critical roles of damping ratios, stiffness coefficients, detuning parameters, and coupling gains in shaping resonance characteristics, multi-valued responses, and stability boundaries. Furthermore, the results confirm that strong electromechanical coupling enhances the broadband harvesting capability, particularly under low-frequency excitations. From a dynamic perspective, the PPF control strategy establishes more stable and predictable operating regimes, which are essential for efficient energy harvesting. Although the electrical circuit is not explicitly modeled, the inherent coupling between mechanical response and electrical output implies that the observed improvements in vibration behavior lead to more stable and effective energy extraction. Although a direct quantitative comparison with other control strategies is beyond the scope of this study, the obtained results indicate that the proposed approach offers improved dynamical performance and enhanced adaptability compared to conventional passive systems. Overall, this work provides a solid bridge between nonlinear analytical modeling and practical applications in vibration control and self-powered sensing systems. Our findings of this study open new directions for the design of controlled nonlinear energy harvesting systems. Moreover, the results indicate that the proposed PPF-based control framework has strong potential for extension to large-scale flexible structures, such as spacecraft systems, where reliable vibration suppression and stability enhancement are essential under complex dynamic conditions.

6.1. Recommendations for improvement

In future work, researchers may focus on extending this study toward more practical and advanced implementations. In particular:

Developing real-time adaptive PPF controllers using established techniques such as online sensing, state estimation (e.g., observer-based approaches), and parameter identification algorithms, enabling the controller to adjust dynamically to varying operating conditions.

Extending this model to multi-degree-of-freedom (multi-DOF) systems to better represent realistic structural configurations and capture more complex vibration modes.

Investigating hybrid energy harvesting mechanisms by integrating piezoelectric systems with other transduction methods, such as electromagnetic or triboelectric harvesting, to enhance overall energy conversion efficiency.

Building on the results obtained in this study, where the PPF controller demonstrates a significant

ability to suppress nonlinear vibrations, eliminate multi-valued responses, and enhance system stability, these extensions are expected to further improve the robustness, adaptability, and practical applicability of the proposed energy harvesting system. These improvements may enable the system to operate efficiently under realistic and time-varying environmental excitations.

Author contributions

Moamen Wafaie: Methodology, software, validation, data curation, reviewing, and editing; Rageh K. Hussein: Investigation, methodology, and formal analysis; Ashraf Taha EL-Sayed: Conceptualization, investigation, resources, software, methodology, writing–original draft preparation, visualization, reviewing and editing; Fatma Taha El-Bahrawy: Investigation, methodology, data curation, validation, reviewing and editing. All authors have read and approved the final version of the manuscript for publication.

Use of Generative-AI tools declaration

The authors declare they have not used Artificial Intelligence (AI) tools in the creation of this article.

Conflict of interest

The authors declare no conflicts of interest.

Appendix

$$M_{11}=-\omega_1\xi_1-\frac{\alpha_2\alpha_3\delta}{2\left(\delta^2+\omega_1^2\right)},\ M_{12}=\frac{f}{2\omega_1}\cos\left(\theta_{10}\right),\ M_{13}=\frac{\gamma_1}{2\omega_1}\sin\left(\theta_{20}\right),\ M_{14}=\frac{\gamma_1}{2\omega_1}a_{20}\cos\left(\theta_{20}\right).$$

$$M_{21}=\frac{\left(\Omega-\omega_1\right)}{a_{10}}+\frac{3\omega_1\beta}{4}a_{10}+\frac{9\alpha_1\omega_1}{8}a_{10}-\frac{\alpha_2\alpha_3\omega_1}{2a_{10}\left(\delta^2+\omega_1^2\right)}.$$

$$M_{22}=-\frac{f}{2a_{10}\omega_1}\sin\left(\theta_{10}\right),\ M_{23}=\frac{\gamma_1}{2a_{10}\omega_1}\cos\left(\theta_{20}\right),\ M_{24}=-\frac{\gamma_1}{2\omega_1a_{10}}a_{20}\sin\left(\theta_{20}\right).$$

$$M_{31}=-\frac{\gamma_2}{2\omega_2}\sin\left(\theta_{20}\right),\ M_{32}=-\omega_2\xi_2,\ M_{33}=0,\ M_{34}=-\frac{\gamma_2}{2\omega_2}a_{10}\cos\left(\theta_{20}\right).$$

$$M_{41}=\frac{\left(\omega_2-\omega_1\right)}{a_{10}}+\frac{3\omega_1\beta}{4}a_{10}+\frac{9\alpha_1\omega_1}{8}a_{10}-\frac{\alpha_2\alpha_3\omega_1}{2\left(\delta^2+\omega_1^2\right)a_{10}}-\frac{\gamma_2}{\omega_2a_{20}}\cos\left(\theta_{20}\right).$$

$$M_{42}=-\frac{f}{2a_{10}\omega_1}\sin\left(\theta_{10}\right).$$

$$M_{43}=\frac{\left(\omega_2-\omega_1\right)}{a_{20}}+\frac{\omega_1\beta}{4a_{20}}a_{10}^2+\frac{3\alpha_1\omega_1}{8a_{20}}a_{10}^2-\frac{\alpha_2\alpha_3\omega_1}{2\left(\delta^2+\omega_1^2\right)a_{20}}+\frac{f}{2\omega_1 a_{10}a_{20}}\cos\left(\theta_{10}\right)+\frac{\gamma_1}{\omega_1 a_{10}}\cos\left(\theta_{20}\right).$$

$$M_{44}=-\left(\frac{\gamma_1}{2\omega_1 a_{10}}a_{20}-\frac{\gamma_2}{2\omega_2 a_{20}}a_{10}\right)\sin\left(\theta_{20}\right).$$

References

1. H. Li, J. Zhou, Q. Sun, W. Chen, J. Zhou, Design of broadband rainwater piezoelectric energy harvester based on multimodal resonance, *Acta Phys. Sin.*, **74** (2025), 147701. https://doi.org/10.7498/aps.74.20250213
2. M. Zhao, S. Liu, R. Yi, R. Song, S. Zhang, Y. Hou, Structural optimization and broadband energy harvesting characteristics of variable-section multimodal piezoelectric energy harvesters, *Smart Mater. Struct.*, **34** (2025), 095033. https://doi.org/10.1088/1361-665X/ae066c
3. S. Wu, Y. Yu, C. Sun, W. Liao, J. Kan, S. Wang, et al., An enhanced broadband piezoelectric energy harvester via elastic amplification structure for multidirectional vibration, *Smart Mater. Struct.*, **33** (2024), 125016. https://doi.org/10.1088/1361-665X/ad860e
4. M. Kh, A. Rezaniakolaie, L. Rosendahl, A broadband macro-fiber-composite piezoelectric energy harvester for higher energy conversion from practical wideband vibrations, *Nano Energy*, **76** (2020), 104978. https://doi.org/10.1016/j.nanoen.2020.104978
5. L. Chen, W. Jiang, Internal resonance energy harvesting, *ASME. J. Appl. Mech.*, **82** (2015), 031004. https://doi.org/10.1115/1.4029606
6. S. Sun, Y. Leng, S. Hur, F. Sun, X. Chen, H. C. Song, et al., Force and stability mechanism analysis of two types of nonlinear mono-stable and multi-stable piezoelectric energy harvesters using cantilever structure and magnetic interaction, *Smart Mater. Struct.*, **32** (2023), 035003. https://doi.org/10.1088/1361-665X/acb1e3
7. T. Tan, Z. Wang, L. Zhang, W. H. Liao, Z. Yan, Piezoelectric autoparametric vibration energy harvesting with chaos control feature, *Mech. Syst. Signal Pr.*, **161** (2021), 107989. https://doi.org/10.1016/j.ymssp.2021.107989
8. Z. Liu, W. Huang, P. Guo, H. Yang, L. Weng, B. Wang, Nonlinear model for magnetostrictive vibration energy harvester considering dynamic forces, *IEEE Sens. J.*, **24** (2024), 16270–16278. https://doi.org/10.1109/JSEN.2024.3384439
9. F. T. El-Bahrawy, R. K. Hussein, A. T. EL-Sayed, M. Wafaie, Piezoelectric harvester proportional–derivative (PHPD) control for nonlinear dynamics reduction in underactuated hybrid systems, *Machines*, **13** (2025), 830. https://doi.org/10.3390/machines13090830
10. E. Omidi, S. N. Mahmoodi, Multimode modified positive position feedback to control a collocated structure, *J. Dyn. Syst.-T ASME*, **137** (2015), 051003. https://doi.org/10.1115/1.4029030
11. L. Jun, Positive position feedback control for high amplitude vibration of a flexible beam to a principal resonance excitation, *Shock Vib.*, **17** (2010), 187–203. https://doi.org/10.3233/SAV-2010-0506
12. G. Cazzulani, C. Ghielmetti, F. Resta, F. Ripamonti, Vibration control of flexible structures with an active modal tuned mass damper, *IFAC Proceedings*, **44** (2011), 5371–5376. https://doi.org/10.3182/20110828-6-IT-1002.02087

13. H. H. Syed, Comparative study between positive position feedback and negative derivative feedback for vibration control of a flexible arm featuring piezoelectric actuator, *Int. J. Adv. Robot. Syst.*, **14** (2017), 1–9. https://doi.org/10.1177/1729881417718801
14. M. A. Trindade, A. Benjeddou, R. Ohayon, Piezoelectric active vibration control of damped sandwich beams, *J. Sound Vib.*, **246** (2001), 653–677. https://doi.org/10.1006/jsvi.2001.3712
15. J. Li, Y. Xue, F. Li, Y. Narita, Active vibration control of functionally graded piezoelectric material plate, *Compos Struct.*, **207** (2018), 509–518. https://doi.org/10.1016/j.compstruct.2018.09.053
16. T. Kamada, T. Fujita, T. Hatayama, T. Arikabe, N. Murai, S. Aizawa, et al., Active vibration control of flexural-shear type frame structures with smart structures using piezoelectric actuators, *Smart Mater. Struct.*, **7** (1998), 479–488. https://doi.org/10.1088/0964-1726/7/4/007
17. M. S. Nima, M. Ahmadian, Modified acceleration feedback for active vibration control of aerospace structures, *Smart Mater. Struct.*, **19** (2010), 065015. https://doi.org/10.1088/0964-1726/19/6/065015
18. Y. Pu, H. Zhou, Z. Meng, Multi-channel adaptive active vibration control of piezoelectric smart plate with online secondary path modelling using PZT patches, *Mech. Syst. Signal Pr.*, **120** (2019), 166–179. https://doi.org/10.1016/j.ymssp.2018.10.019
19. P. Kumar, S. Narayanan, S. Gupta, Investigations on the bifurcation of a noisy Duffing–van der Pol oscillator, *Probabilist. Eng. Mech.*, **45** (2016), 70–86. https://doi.org/10.1016/j.probengmech.2016.03.003
20. H. Abdelhafez, M. Nassar, Suppression of vibrations of a forced and self-excited nonlinear beam by using positive position feedback controller PPF, *J. Adv. Math. Comput. Sci.*, **17** (2016), 1–19. https://doi.org/10.9734/BJMCS/2016/26871
21. W. A. El-Ganaini, N. A. Saeed, M. Eissa, Positive position feedback (PPF) controller for suppression of nonlinear system vibration, *Nonlinear Dynam.*, **72** (2013), 517–537. https://doi.org/10.1007/s11071-012-0731-5
22. Y. A. Amer, A. T. El-Sayed, F. T. El-Bahrawy**,** Positive position feedback controllers for reduction the vibration of a nonlinear spring pendulum, *Adv. Math.*, **12** (2016), 6758–6772. https://doi.org/10.24297/jam.v12i11.7
23. H. Bauomy, A. T. El-Sayed, A. M. Salem, F. T. El-Bahrawy**,** The improved giant magnetostrictive actuator oscillations via positive position feedback damper, *AIMS Math.*, **8** (2023), 16864–16886. https://doi.org/10.3934/math.2023862
24. K. Alluhydan, A. T. El-Sayed, F. T. El-Bahrawy**,** The effect of proportional, proportional-integral, and proportional-integral-derivative controllers on improving the performance of torsional vibrations on a dynamical system, *Computation*, **12** (2024), 157. https://doi.org/10.3390/computation12080157
25. H. S. Bauomy, A. T. El-Sayed, F. T. El-Bahrawy, Integral resonant negative derivative feedback suppression control strategy for nonlinear dynamic vibration behavior model, *Chaos Soliton. Fract.*, **189** (2024), 115686. https://doi.org/10.1016/j.chaos.2024.115686
26. T. S. Amer, S. A. Abdelhfeez, F. R. Elbaz, M. K. Abohamer, Investigation of the dynamical analysis, stability, and bifurcation for a connected damped oscillator with a piezoelectric harvester, *J. Vib. Eng. Technol.*, **13** (2025), 155. https://doi.org/10.1007/s42417-024-01641-4
27. C. J. Xu, Y. S. Wu, Bifurcation control for a duffing oscillator with delayed velocity feedback, *Int. J. Autom. Comput*., **13** (2016), 596–606. https://doi.org/10.1007/s11633-015-0944-4

28. F. Qian, S. Zhou, L. Zuo, Approximate solutions and their stability of a broadband piezoelectric energy harvester with a tunable potential function, *Commun. Nonlinear Sci.*, **80** (2020), 104984. https://doi.org/10.1016/j.cnsns.2019.104984
29. A. H. Nayfeh, *Perturbation methods*, New York: Wiley, 2000. https://doi.org/10.1002/9783527617609
30. A. H. Nayfeh, D. T. Mook, *Nonlinear oscillations*, New York: Wiley, 1995. https://doi.org/10.1002/9783527617586
31. R.V. Dukkipati, *Solving vibration analysis problems using MATLAB*, New Delhi: New Age International Pvt. Ltd. Publishers, 2007. Available from: https://civilnode.com/download-book/10279230858031/solving-vibration-analysis-problems-using-matlab.
32. Y. Chen, J. H. Yang, T. Nan, X. D. Yang, K. Lu, F. Liang, Advances in dynamics of fluid-conveying pipes: Model, strategy and experiment, *Int. J. Mech. Sci.*, **312** (2026), 111241. https://doi.org/10.1016/j.ijmecsci.2026.111241
33. C. L. Yue, J. Zhang, K. Shi, Active disturbance rejection control for delayed electromagnetic docking of spacecraft in elliptical orbits, *IEEE T. Aero. Elec. Sys.*, **58** (2022), 2257–2268. https://doi.org/10.1109/TAES.2021.3130830
34. X. Q. Fang, Y. H. Zou, Q. L. He, Nonlinear vibration of five-layered functionally graded piezoelectric semiconductor nano-plate on Pasternak foundation, *Mech. Based Des. Struct.*, **52** (2024), 10761–10782. https://doi.org/10.1080/15397734.2024.2362913

AIMS Press